



Reducing structural degradation of high-voltage single-crystal Ni-rich cathode through in situ doping strategy

Xin-Ming Fan, Zhi Zhang*¹, Gao-Qiang Mao, Ying-Jie Tong,
Ke-Bo Lin, Hui Tong*², Wei-Feng Wei, Qing-Hua Tian, Xue-Yi Guo*³

Received: 24 July 2022 / Revised: 17 August 2022 / Accepted: 29 August 2022 / Published online: 14 July 2023
© Youke Publishing Co., Ltd. 2023

Abstract Polycrystalline Ni-rich layered oxide ($\text{LiNi}_x\text{Co}_y\text{Mn}_z\text{O}_2$ (NCM), $x > 0.8$) cathode material with high specific capacity and low cost is considered as one of the most promising candidate materials for lithium-ion batteries (LIBs). However, it suffers from severe structural and capacity degradation during practical cycling, especially under harsh operation condition (ultrahigh cutoff voltage and elevated temperature, etc.). One promising approach to mitigate these issues is to develop a single-crystal Ni-rich NCM cathode, which could enhance structural integrity and improve capacity retention, due to its robust and stable micro-sized primary particles. However, the improved cyclic stability comes at the expense of reversible capacity and rate capability, owing to the relatively low Li^+ diffusion efficiency for its micron-sized primary particles. Moreover, the structural degradation and exacerbation of interfacial reactions for the Ni-rich NCM cathode under high-voltage (≥ 4.5 V) would quickly trigger the poor electrochemical performance, limiting its practical applications. Herein, $\text{LiNi}_{0.827}\text{Co}_{0.11}\text{Zr}_{0.003}\text{Mn}_{0.06}\text{O}_2$ (Zr@SC- N_{83}) cathode

material was successfully synthesized via the in situ doping strategy. It could not only effectively maintain the reversibility of phase transition between H2 and H3 after long-term cycling at high voltage (4.6 V), but also enhance lithium-ion diffusion, thus improving the cycling performance and good rate performance for the Zr@SC- N_{83} cathode. As a result, 0.3 wt% Zr-doping cathode delivers an initial discharging capacity of 200.1 $\text{mAh}\cdot\text{g}^{-1}$ at 1.0C and at the high cutoff voltage of 4.6 V, exhibiting the satisfactory capacity retention of 85.5% after 100 cycles. It provides an effective route toward low-cost and higher energy density for lithium-ion batteries with Ni-rich cathode.

Keywords Single-crystal Ni-rich $\text{LiNi}_x\text{Co}_y\text{Mn}_z\text{O}_2$ (NCM); In situ doping strategy; High voltage; Structural integrity; Cycling stability

1 Introduction

With the wide application of Li-ion batteries in electric vehicles and energy storage systems, the demand of developing the high performance of cathodes for the high energy

Supplementary Information The online version contains supplementary material available at <https://doi.org/10.1007/s12598-023-02288-y>.

X.-M. Fan, W.-F. Wei
Powder Metallurgy Research Institute, Central South University,
Changsha 410083, China

X.-M. Fan, G.-Q. Mao, Y.-J. Tong, K.-B. Lin, H. Tong*,
Q.-H. Tian, X.-Y. Guo*
School of Metallurgy and Environment, Central South
University, Changsha 410083, China
e-mail: huitong@csu.edu.cn

X.-Y. Guo
e-mail: xyguo@csu.edu.cn

X.-M. Fan, H. Tong, Q.-H. Tian, X.-Y. Guo
National & Regional Joint Engineering Research Center of
Nonferrous Metal Resource Recycling, Changsha 410083, China

X.-M. Fan, H. Tong, Q.-H. Tian, X.-Y. Guo
Engineering Research Center of the Ministry of Education for
Advanced Battery Materials, Central South University,
Changsha 410083, China

Z. Zhang*
College of Chemistry and Materials Engineering, Hunan
University of Arts and Science, Changde 415000, China
e-mail: Zhangzhi@huas.edu.cn



density and long-life span batteries is gradually increasing [1–3]. As a candidate, the conventional Ni-rich layered oxide cathode ($\text{LiNi}_x\text{Co}_y\text{Mn}_z\text{O}_2$ (NCM), $x > 0.8$) is regarded as the auspicious cathode material, due to its attractive reversible capacity ($> 200 \text{ mAh}\cdot\text{g}^{-1}$) [4–6]. However, the polycrystalline Ni-rich layered oxide cathodes (PC-NCM) are prone to structural degradation and severe side reaction during the long-term cycling process, resulting in battery performance deterioration [7–13]. In addition, the formation of surface residual lithium species (LiOH and Li_2CO_3) could block lithium diffusion and decrease the reversible capacity [14–18]. Severe impedance growth during the charging-discharging process ultimately causes the increased polarization and substantial safety issues [19, 20].

To address these issues, extensive efforts have been carried out to improve the cycle performance of NCM in high-voltage operation [11, 21–26], including elemental doping (Mg, Al, Ti, Sn, etc.) and surface coatings (Al_2O_3 , AlPO_4 and Li_3PO_4 , etc.). However, the vital defects of severe intergranular cracks for the PC-NCM cathode materials are still inevitable, especially under harsh operating conditions (the elevated temperature and high cutoff voltage, etc.). In our previous works, the capacity retention of the single crystal NCM (SC-NCM) cathode is superior to that of PC-NCM cathode, due to its robust structure and fewer grain boundaries [27–32]. It means that the micron-sized primary particles of SC-NCM cathodes could effectively suppress the micron scale structural degradation, including the appearance of intergranular cracks. In addition, with the increase in the charging cutoff voltage, SC-NCM cathodes could release more Li^+ and possess higher specific capacity value, which is becoming a research hot spot in academia and industry. Nevertheless, the interfacial instability and bulk structural degradation of the Ni-rich SC-NCM cathodes at high operation potentials would cause rapid capacity decay and voltage fading. Therefore, it still has a great challenge to develop the high-voltage Ni-rich SC-NCM ($\text{Ni} > 0.8$) cathodes with superb cycling stability and the high capacity at high voltage ($\geq 4.6 \text{ V}$).

The foreign elements doping in the SC-NCM cathode could be an effective way to restrict the internal stress at a deep discharging state [33–35]. However, the current doping strategies are commonly executed by the after-treatment, making it challenging to ensure a uniform distribution of foreign element ions in the bulk of SC-NCM material. Meanwhile, the relevant electrochemical performances of the doping cathode materials with the different treatments are seldom discussed in the literature, which plays a crucial role in the enhanced structural stability and electrochemical performances of the SC-NCM cathodes.

In this work, a Zr-doped Ni-rich single-crystalline $\text{LiNi}_{0.827}\text{Co}_{0.11}\text{Mn}_{0.06}\text{Zr}_{0.003}\text{O}_2$ (Zr@SC-N₈₃) material was synthesized by in situ doping method. The introduction of trace Zr element exhibits the following positive effects: (1) effectively enhancing electrochemical reactivity; (2) bulk doping improves the structural stability; (3) inhibiting the side reactions with the uniformly surface distribution of Zr^{4+} ; (4) improving Li^+ transportation via increasing the interlayer distance. The positive effects of Zr-doping in the surface and bulk of SC-NCM cathode material could enable better electrochemical performances, compared with the undoped sample.

2 Experimental

2.1 Synthesis of Zr@SC-N₈₃ material

The spherical precursor $\text{Ni}_{0.827}\text{Co}_{0.11}\text{Mn}_{0.06}\text{Zr}_{0.003}(\text{OH})_2$ of Zr@SC-N₈₃ samples were synthesized via a co-precipitation method [28, 36]. A stoichiometric amount of $\text{NiSO}_4\cdot 6\text{H}_2\text{O}$, $\text{CoSO}_4\cdot 7\text{H}_2\text{O}$, and $\text{MnSO}_4\cdot 5\text{H}_2\text{O}$ (the concentrations for all samples are $2 \text{ mol}\cdot\text{L}^{-1}$) solution were pumped into the reaction tank. $\text{Zr}(\text{SO}_4)_2\cdot 4\text{H}_2\text{O}$ ($0.5 \text{ mol}\cdot\text{L}^{-1}$), NaOH ($5 \text{ mol}\cdot\text{L}^{-1}$, the precipitation agent), and $\text{NH}_3\cdot\text{H}_2\text{O}$ ($4 \text{ mol}\cdot\text{L}^{-1}$, chelating agent) solutions were separately pumped into the tank reactor as mentioned above under N_2 atmosphere. After filtering the precipitations, washing, and drying, the as-prepared precursor was finally heated in a vacuum oven at $120 \text{ }^\circ\text{C}$ for 12 h. The precursor was thoroughly mixed with $\text{LiOH}\cdot\text{H}_2\text{O}$ (M:Li ratio = 1:1.06, where M represents Ni/Co/Mn ions) and subsequently calcined at $500 \text{ }^\circ\text{C}$ for 6 h. Finally, the Zr@SC-N₈₃ materials are obtained to calcine at $830 \text{ }^\circ\text{C}$ for 10 h in an oxygen atmosphere. For comparison, the bare $\text{LiNi}_{0.83}\text{Co}_{0.11}\text{Mn}_{0.06}\text{O}_2$ (SC-N₈₃) samples were fabricated by a similar method without adding the Zr containing salt. Besides, the after-treated Zr@SC-N₈₃ samples were prepared by doping after precursor synthesis.

2.2 Material characterization

Chemical compositions of Zr@SC-N₈₃ particles were tested by inductively coupled plasma optical emission spectrometry (OPIMA 8300, Perkin Elmer). Crystalline structures of all samples were determined by X-ray diffraction measurement (XRD, PANalytical Empyrean), where 2θ was corrected from 5° to 120° at $2 \text{ (}^\circ\text{)}\cdot\text{min}^{-1}$ and transmission electron microscopy (TEM, JEOL 2100F, JEOL). In addition, X-ray photoelectron spectroscopy

(XPS) tests of all samples were conducted by Thermo Fisher ESCALAB 250Xi. Before XPS testing, the cycled cathodes were washed with dimethyl carbonate (DMC) three times.

2.3 Electrochemical measurements

The cathode slurry containing the active materials, acetylene black, and polyvinylidene fluoride (PVDF) at a weight ratio of 8:1:1 was coated on aluminum foil, where the area loading of the active material is about $8.0 \text{ mg}\cdot\text{cm}^{-2}$. Coin-type cell (CR2032) was assembled with a lithium metal anode, the prepared Zr@SC-N₈₃ cathode, and a commercial electrolyte of $1.0 \text{ mol}\cdot\text{L}^{-1}$ LiPF₆ in ethylene carbonate/ethyl methyl carbonate/diethyl carbonate (EC/EMC/DEC, LB037 obtained from DoDo Chemical Co., Ltd, Soochow, China). A LAND battery cyclor was applied to test the cycling performances of the cells at 2.75–4.6 V (vs. Li/Li⁺) and 25 °C. A CHI660D electrochemical station (Chenhua, Shanghai) was employed to acquire electrochemical impedance spectra (EIS) over the frequency range of 1×10^{-2} – 1×10^5 Hz at

25 °C. The state of charge of the cells for EIS, XPS, SEM and TEM measurements are the fully discharging state.

3 Results and discussion

3.1 Morphology and composition

The representative electron microscopy images of the as-prepared Ni_{0.827}Co_{0.11}Mn_{0.06}Zr_{0.003}(OH)₂ precursor and Zr@SC-N₈₃ material are shown in Fig. 1. The precursor consists of aggregated particles and shows an apparent secondary particle of 3.5–5.5 μm (Fig. 1a). After the modified solid-state reaction at high temperature, Zr@SC-N₈₃ cathode material exhibited micron-sized polyhedral particles with a smooth surface (Fig. 1c), similar to bare SC-N₈₃ particles (Fig. 1b). To verify the uniformity of element distribution, the Zr@SC-N₈₃ sample was examined by EDS mapping (Fig. 1d). Ni, Co, Mn and Zr elements were uniformly distributed on the surface of Zr@SC-N₈₃ particles. SEM–EDS line scanning of the cross-section for the Zr@SC-N₈₃ primary particle further

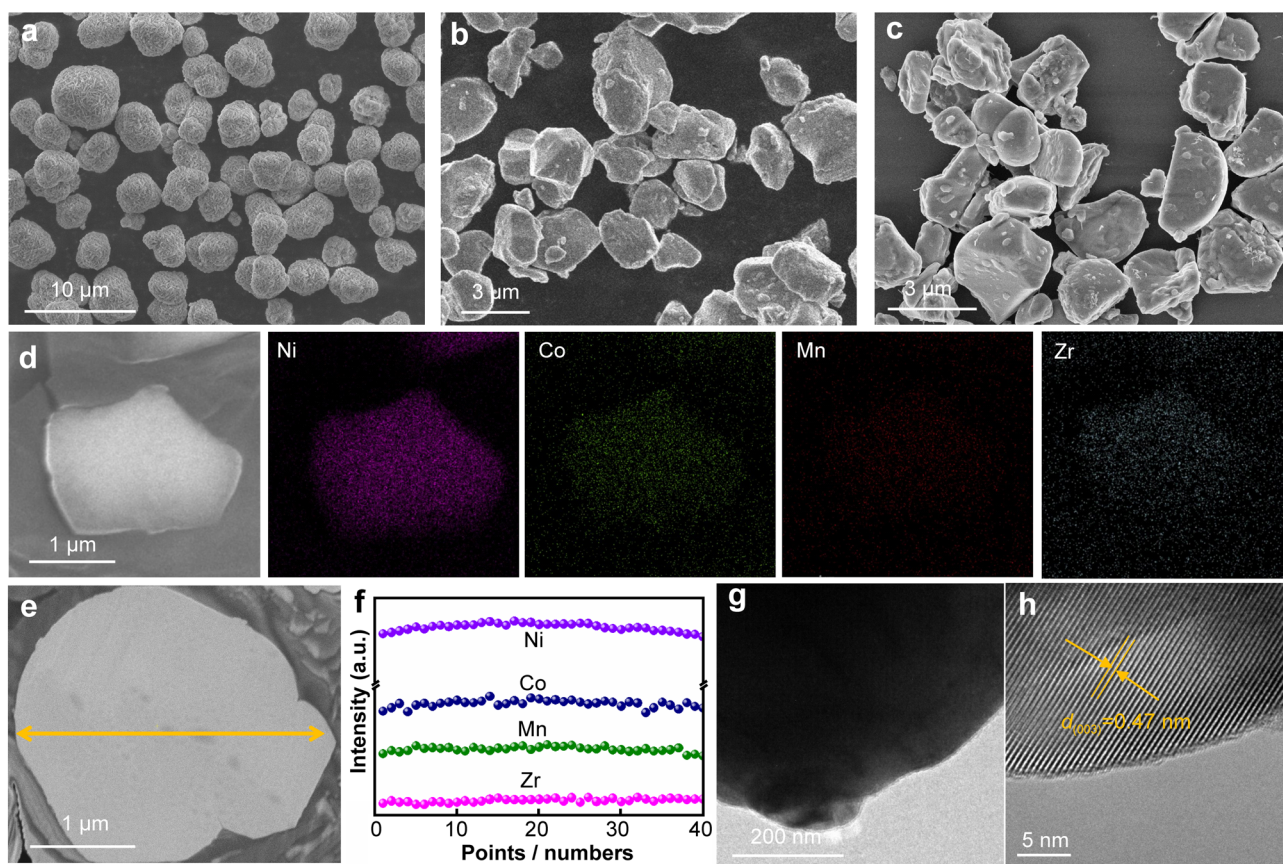


Fig. 1 SEM images of **a** precursor, **b** bare SC-N₈₃ and **c** Zr@SC-N₈₃ materials; **d** SEM image and corresponding elemental mappings of a single Zr@SC-N₈₃ particle; **e** cross-section SEM image of a single Zr@SC-N₈₃ particle and **f** corresponding EDS linear scan mapping of transition metal elements; **g**, **h** HRTEM images of a Zr@SC-N₈₃ particle

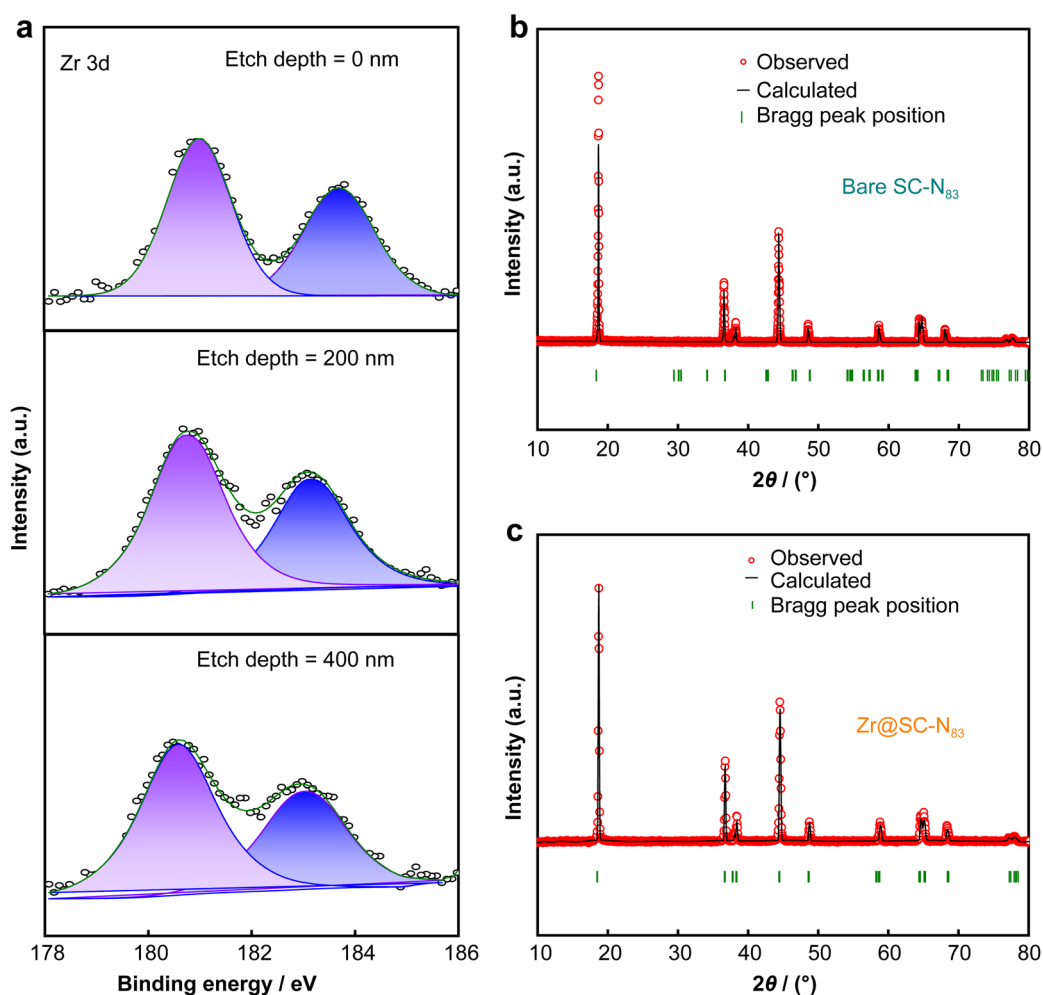


Fig. 2 a XPS results of Zr 3d for Zr@SC-N₈₃, b, c XRD pattern and Rietveld refinement results of bare SC-N₈₃ and Zr@SC-N₈₃ materials

demonstrates that Zr ions are doped into the bulk particle (Fig. 1e, f). It means that the transition metal ions in Zr@SC-N₈₃ lattice were substituted by Zr⁴⁺, which could mitigate the parasitic reaction at the electrode/electrolyte interface and improve the structural stability. The corresponding HRTEM images in Fig. 1g, h show a precise and uniform interplanar distance of 0.47 nm, corresponding to (003) crystal planes of the layered structure of NCM.

Moreover, XPS spectrum and XRD diffraction patterns of the bare SC-N₈₃ and Zr@SC-N₈₃ samples are shown in Fig. 2 and Table S1. Two peaks of Zr 3d of Zr@SC-N₈₃ material at different etch depths (0, 200 and 400 nm) from particle surface are located at 181.59 and 183.98 eV, respectively (Fig. 2a). And the intensity of Zr from the outer surface to the interior of Zr@SC-N₈₃ is almost the same. It suggests that Zr is homogeneous distribution, which is consistent with by cross section SEM-EDS mapping and liner scanning. In addition, XRD patterns of Zr@SC-N₈₃ powder (Fig. 2b, c and Table S2) could be

corresponding to the typical layered hexagonal structures with a space group *R-3m* (JCPDS No. 87-1562), which exhibits the marked splitting of pair reflections (006)/(102) and (108)/(110) [37, 38]. In general, Zr⁴⁺ doping with the relatively large ion radius (0.072 nm) could stable the structural stability of NCM materials and increase the lithium ion transportation during cycling process. Therefore, it could be a good method to improve the cycle performance of the Zr@SC-N₈₃ sample, especially at the elevated cutoff voltage.

3.2 Electrochemical test

To reveal the fundamental effects of Zr⁴⁺ doping, a series of electrochemical tests were performed at 2.75–4.6 V in 2032-type coin cells with the Zr@SC-N₈₃ and the bare SC-N₈₃ cathodes in Fig. 3. Figure 3a displays the initial charge-discharge profiles of the Zr@SC-N₈₃ and the bare SC-N₈₃ cathodes at 2.75–4.6 V and 0.1C. In detail, the

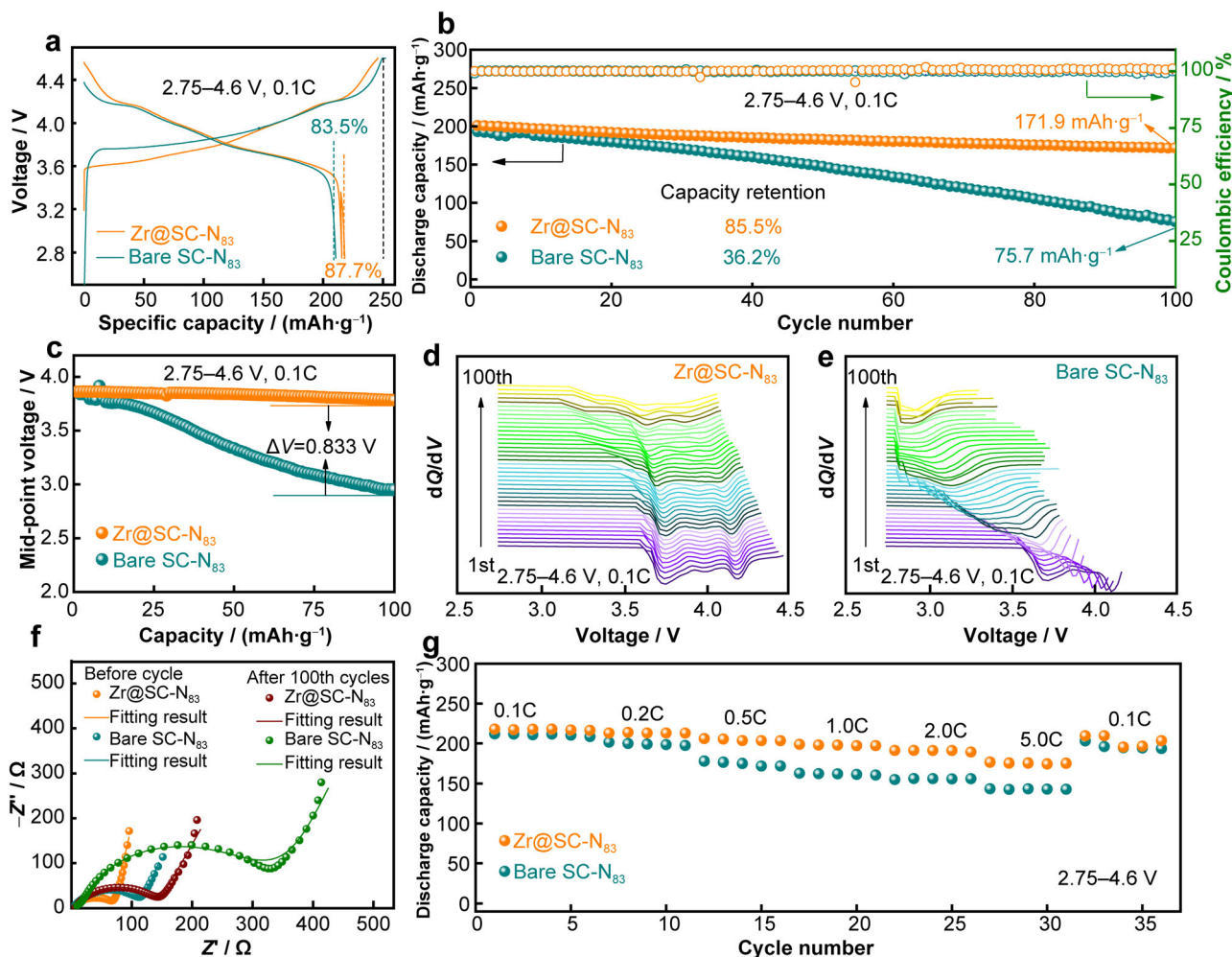


Fig. 3 Electrochemical performances of Zr@SC-N₈₃ and bare SC-N₈₃ cathodes at 2.75–4.6 V: **a** initial charge–discharge curves at 0.1C; **b** cycle performance at 1.0C; **c–e** corresponding midpoint voltage and dQ/dV curves during 100 cycles at 1.0C; **f** EIS results before cycling and after 100 cycles at 1.0C (Z' stands for real part impedance, Z'' stands for imaginary part impedance); **g** rate performance of these cathodes at 0.1C to 5.0C

charge-discharge curves for both cathodes display similar shapes, indicating that no extra electrochemical reaction occurred after in situ Zr⁴⁺-doping treatment. Both the Zr@SC-N₈₃ and bare SC-N₈₃ cathodes exhibit the similar initial discharge capacity (about 218 and 210.5 mAh·g⁻¹, respectively) at 2.75–4.6 V/0.1C. Moreover, the Coulombic efficiency of the Zr@SC-N₈₃ cathode at initial cycle is slightly larger than that of the bare SC-N₈₃ cathode, which is attributed to the enhanced reversibility of phase transition between H2 and H3 after Zr⁴⁺-doping. Notably, the Zr@SC-N₈₃ cathode exhibits a higher discharge capacity of 171.9 mAh·g⁻¹ after 100 cycles at 1.0C and 2.75–4.6 V in Fig. 3b, maintaining satisfactory capacity retention of 85.5%, which is superior to that of the bare SC-N₈₃ cathode (75.7 mAh·g⁻¹ and 36.2%, respectively). The significantly enhanced cycling stability of the Zr@SC-N₈₃ cathode might be ascribed to Zr⁴⁺ doping, providing additional Li⁺

deintercalation channels that reduce the irreversible specific capacity losses and electrochemical polarization voltages [39]. Furthermore, the different contents of the Zr-doping in Zr@SC-N₈₃ cathodes and the after-treated Zr-doped SC-N₈₃ (noted as the Zr/SC-N₈₃) were adjusted to achieve the optimized electrochemical performance in Fig. S1, which shows that the best cycling stability is obtained by 0.3 wt% Zr doped into the SC-N₈₃ cathode. It also exhibits the comparable results at such high voltage in literature (Table S4), demonstrating the best cycling stability at 4.6 V. Besides, the Zr@SC-N₈₃ cathode shows the fast lithium-ion diffusion kinetics, compared to the bare SC-N₈₃ cathode, according to the EIS fitting results (Fig. 3f and Table S3). It is well known that the more considerable D_{Li^+} (lithium-ion diffusion coefficients) value indicates the faster lithium-ion diffusivity. Therefore, the Zr@SC-N₈₃ cathode could significantly reduce the electrochemical

resistance of batteries during cycling process, which is also consistent with the changes in midpoint voltage values during 100 cycles for these two samples. As shown in Fig. 3c, the SC-N₈₃ cathode exhibits the fast mid-voltage values decay as increasing cycles, speculating the severe structural degradation. In contrast, the smaller polarization voltage is achieved after the Zr-doping ($\Delta V = 0.833$ V, ΔV stands for the midpoint voltage difference between the SC-N₈₃ cathode and the Zr@SC-N₈₃ after 100 cycles at 2.75–4.6 V), indicating the better cycling stability for the Zr@SC-N₈₃ cathode. Additionally, the corresponding differential capacity (dQ/dV) profiles under different voltage platforms are analyzed in Fig. 3e. For the bare SC-N₈₃ electrode, the cathode peak sharply moves out of the voltage window with the decrease of peak intensity. Finally, it disappears during the cycling process, which might be caused by electrode polarization. At the same time, with the continuously left shift of the cathodic peak at 3.75–4.0 V, a rapid decrease of the initial discharge voltage can be observed during the cycle, indicating that the bare SC-N₈₃ cathode had a severe polarization behavior and rapid capacity decline. On the contrary, the cathodic peak of the Zr@SC-N₈₃ electrode exhibits a negligible attenuation after 100 cycles, as shown in Fig. 3d. It is further demonstrated that the polarization behavior of Zr@SC-N₈₃ is effectively inhibited, significantly reducing the parasitic reactions at the electrode/electrolyte interface and improving the structural integrity of the Zr@SC-N₈₃ electrode at ultrahigh cutoff voltage of 4.6 V.

To investigate the interfacial reaction kinetics of the Zr@SC-N₈₃ and the bare SC-N₈₃ cathodes, EIS measurements results of these two samples before and after 100 cycles are shown in Fig. 3f and EIS results are simulated using the equivalent circuit plots (Fig. S2). All Nyquist plots consist of a depressed semicircle at high frequency and a slope at low frequency, corresponding to the charge-transfer resistance at the electrode–electrolyte interface (R_{ct}) and Warburg impedance, respectively. The values of the fitting resistance for the bare SC-N₈₃ and Zr@SC-N₈₃ cathodes before and after 100 cycles are listed in Table S3. R_{ct} values of the SC-N₈₃ and Zr@SC-N₈₃ cathodes are 151.4 Ω /95.54 Ω (before cycle) and 461.22 Ω /194 Ω (after 100 cycles), respectively. The more negligible impedance of the Zr@SC-N₈₃ cathode confirms that the effect of Zr-doping can reduce the resistance at the electrode–electrolyte interface, thus enhancing the electrochemical performance. The corresponding D_{Li^+} are calculated by the following formula and listed in Table S3, where the detail values of the bare SC-N₈₃ and Zr@SC-N₈₃ cathodes are 4.53×10^{-13} and 1.50×10^{-12} before cycles, and 6.17×10^{-14} and 9.69×10^{-14} cm²·s⁻¹ after 100 cycles, respectively. It means that the Zr-doped modified SC-N₈₃ material exhibits a higher Li-ion diffusion coefficient than

the bare Ni-rich NCM material before and after cycling, which is consistent with the results of the cycling performance.

As the current density increases, the Zr@SC-N₈₃ cathode delivers a better rate performance at 0.1C, 0.2C, 0.5C, 1.0C, 2.0C and 5.0C, compared with the bare SC-N₈₃ cathode (Fig. 3g). Both samples delivered similar discharge capacities at 0.1C and 0.2C. Nevertheless, with the lifting of the current density, the difference in discharge capacity value for the bare SC-N₈₃ and Zr@SC-N₈₃ cathodes is increasing rapidly. Especially at the current rate of 5.0C, the Zr@SC-N₈₃ sample also exhibits a higher capacity of 175.6 mAh·g⁻¹, compared to that of the bare SC-N₈₃ cathode (143.4 mAh·g⁻¹). It is worth noting that the foreign Zr-doping modification strategy could effectively improve the rate capability of the SC-N₈₃ cathode due to its more significant lithium diffusion coefficient and the relatively low mitigated side reactions at the electrode/electrolyte interface. Therefore, the excellent comprehensive electrochemical performance of the Zr@SC-N₈₃ cathode is contributed to improving the structural stability and inhibiting side reactions.

It is well known that crack formation and surface deterioration would play a critical role in the battery performance, especially during the charging-discharging process at high voltage [27–29]. First of all, nano/micro-cracks may quickly occur at the vast volume shrinkage and expansion during the H2-H3 phase transition beyond 4.2 V, influencing the structural integrity. On the other hand, high-voltage induced electrolyte decomposition may attack the cathode material surface, forming a vulnerable cathode–electrolyte interface. Zr-modification strategy could provide an effective way to address these issues. The morphologies of the cycled bare SC-N₈₃ and Zr@SC-N₈₃ particles after 100 cycles at 4.6 V and 1.0C reveal this positive effect of the Zr-doping (Fig. 4). As shown in Fig. 4e–g, the microstructure of the bare SC-N₈₃ particle becomes quite different after cycling, where some severe intergranular cracks are observed. It implies that the high reactivity of Ni³⁺ would lead to structural instability, causing the intergranular cracks associated with the surface structural degradation. On the other hand, this phase evolution and structural deformation are almost immunized by the Zr@SC-N₈₃ electrodes. In detail, the intergranular cracks for the Zr@SC-N₈₃ electrode have practically disappeared on both the internal and external surfaces of the particles (Fig. 4a–c). It is demonstrated that the structural integrity of the micron-sized particle for the Zr@SC-N₈₃ electrode is well maintained, indicating that Zr can serve as a substitution of transition metal and inhibit the undesired crack formation and surface deterioration. Moreover, the SEM–EDS mapping signals of the C, O, F and P elements of the Zr@SC-N₈₃ electrode are slightly weaker than that

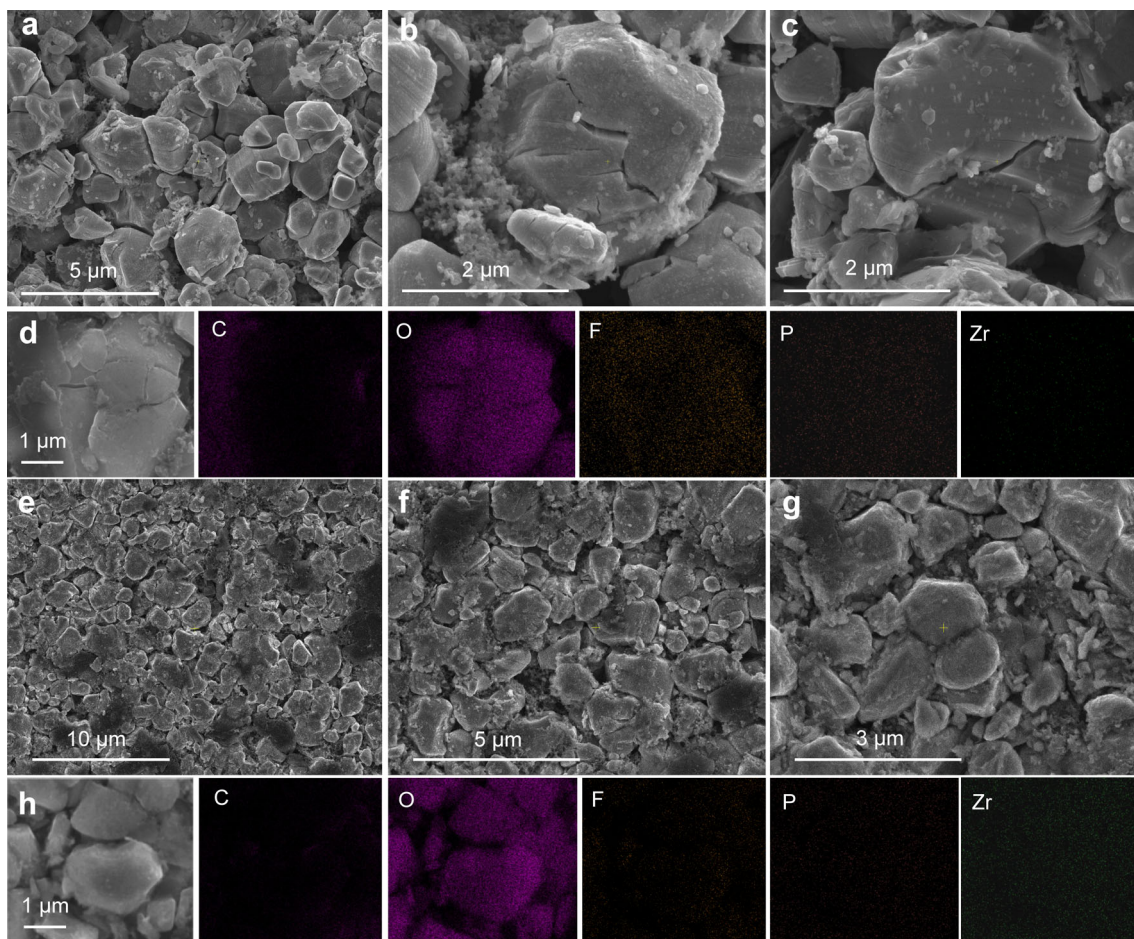


Fig. 4 SEM images and EDS mapping images of **a–d** bare SC-N₈₃ and **e–h** Zr@SC-N₈₃ cathodes after 100 cycles at 2.75–4.6 V and 1.0C

on the surface of the bare SC-N₈₃ electrode, displaying the relatively low content of the electrolyte decomposition after Zr-doping. Meanwhile, the presence of the Zr with a larger ionic radius in the SC-N₈₃ electrode kinetically facilitates the Li⁺ diffusion, thus improving the excellent cell-level electrochemical performance, even exceed to the reported SC-NCM at high-voltage in literature (Table S4).

3.3 Morphologies and composition after long-term cycling

To further demonstrate the inhibiting effect of the electrolyte decomposition on the Zr@SC-N₈₃ cathode surface, the cycled cells with the bare SC-N₈₃ and Zr@SC-N₈₃ cathodes were disassembled in the glove box, and the washed cathodes were tested by XPS measurement (Fig. 5). The cathode/electrolyte interfacial (CEI) chemistry on both samples includes the carbon, oxygen, fluorine, and phosphorous species, where analysis of individual spectra reveals the slight differences in concentrations. In Fig. 5a, C 1s data show the evidence of four distinct

carbon-containing compounds with binding energies at 284.2, 286.5, 287.7 and 290.5 eV, respectively, corresponding to C–C, C–O, C=O and OCO₂ species from the decomposition of carbonate solvents (such as EC, EMC and DEC) [40]. The concentration of carbon-containing species reduces after Zr-doping, indicating that the decomposition ratio of the carbonate solvent is small, which is well consistent with the O 1s spectra (Fig. 5b). F 1s and P 2p data for these two cathodes are mainly dominated by LiF (684.8 eV) and LiPO_xF_y (133.2 eV) compounds [41, 42]. Moreover, the lower concentration of these two species in F 1s and P 2p spectra for the Zr@SC-N₈₃ cathode is observed in Fig. 5c, d, demonstrating the lower decomposition concentration of LiPF₆. It indicates that the distribution of trace Zr on the surface and bulk of the SC-N₈₃ cathode can reduce the electrolyte decomposition deposits on the cathode surface, forming a thin and low impedance (Fig. 3f) of CEI film.

TEM analysis further revealed the suppression of structural degradation of the Zr@SC-N₈₃ electrode (Fig. 6a–g). As shown in Fig. 6a, there are severe cracks in

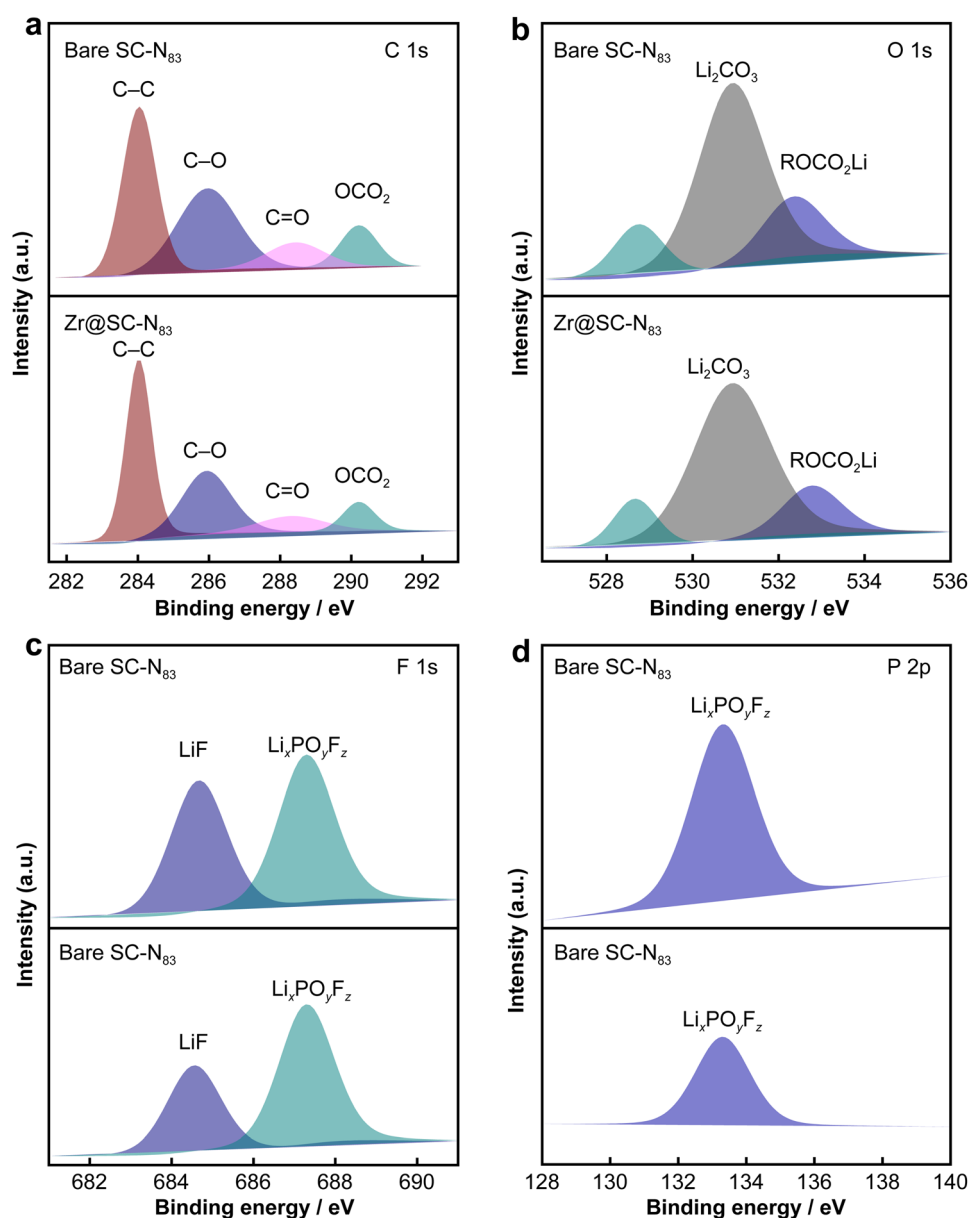


Fig. 5 XPS spectra of **a** C 1s, **b** O 1s, **c** F 1s and **d** P 2p for cycled bare SC-N₈₃ and Zr@SC-N₈₃ cathodes after 100 cycles at 2.75–4.6 V and 1.0C

the surface of the bare SC-N₈₃ particle (Fig. 6a). Meanwhile, the structural integrity is observed in TEM images of the Zr@SC-N₈₃ particle after long-term cycling at 4.6 V (Fig. 6d). This phenomenon is also revealed by SEM images of the cycled electrodes in Fig. 4, which further confirms the better mechanical stability after Zr-doping. HRTEM images display the surface of the bare SC-N₈₃ (Fig. 6b) and Zr@SC-N₈₃ (Fig. 6e) particles after 100 cycles. The surface region of the bare SC-N₈₃ particle (yellow, cubic region) changes into a NiO phase with a thickness of more than 21 nm (Fig. 6b). The transition-

metal ions have migrated to the lithium layer. The thick rock-salt phases of the cycled SC-N₈₃ electrode are also confirmed by fast Fourier transformation (FFT) in Fig. 6c. By contrast, the slight surface degradation (NiO layer is about ~ 7 nm) of the cycled Zr@SC-N₈₃ cathode is confirmed by HRTEM and FFT images (Fig. 6e–g), further indicating that the Zr-doping method can effectively inhibit the reversible phase transition.

The operation mechanism of the bare SC-N₈₃ and Zr@SC-N₈₃ cathodes at a high-voltage of 4.6 V is elaborated in Fig. 6h. For the SC-N₈₃ electrode, Zr doping can

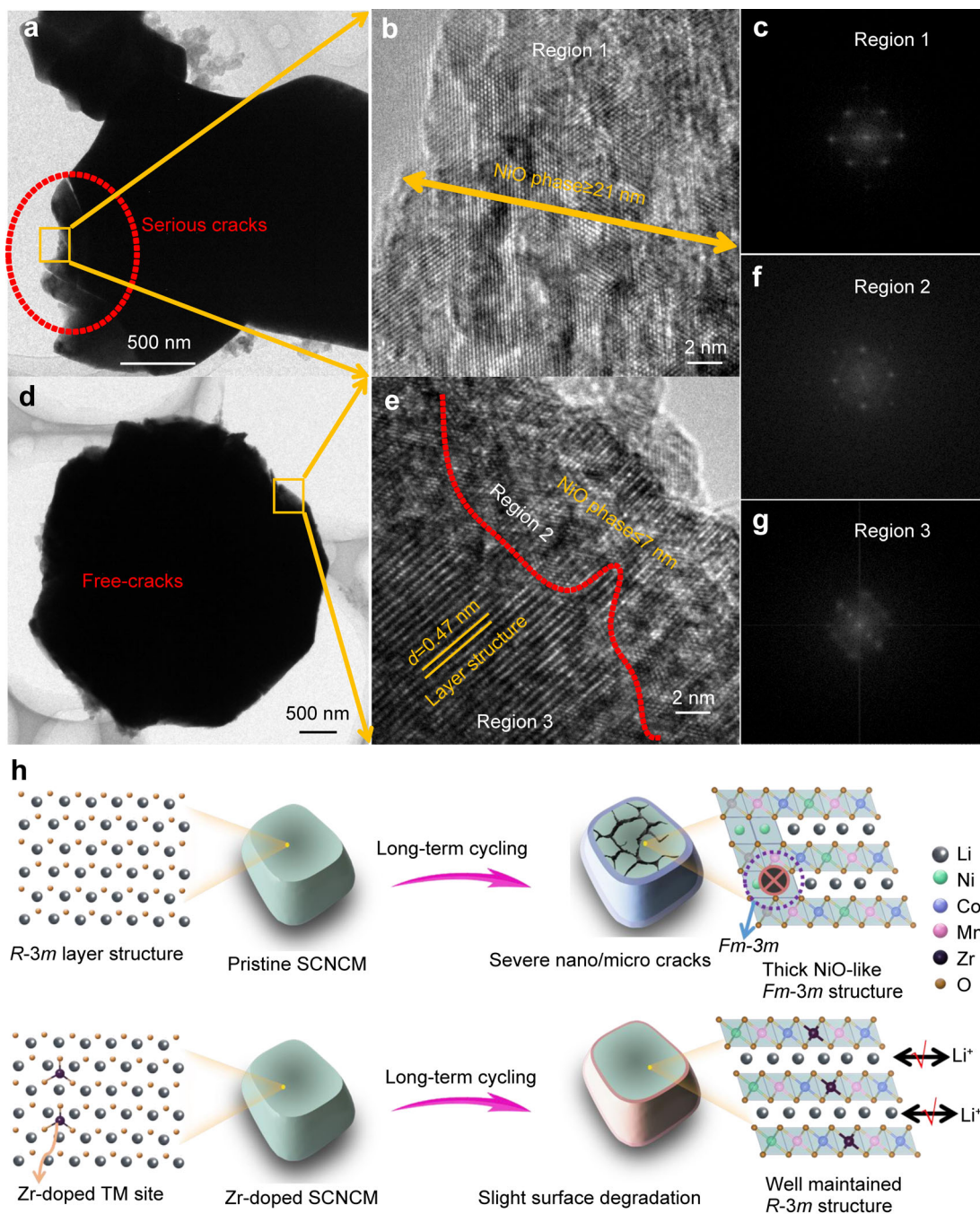


Fig. 6 TEM images of **a, b** bare SC-N₈₃ and **d, e** Zr@SC-N₈₃ cathodes after 100 cycles; corresponding FFTs of **c** Region 1 in bare SC-N₈₃ and; **f, g** Regions 2, 3 in Zr@SC-N₈₃ cathodes; **h** operation mechanism of bare SC-N₈₃ and Zr@SC-N₈₃ samples at high-voltage of 4.6 V

not only enhance the Li⁺ transportation, but also enhance the structural stability, thus improving the electrochemical performance of the battery. However, the bare SC-N₈₃ electrode underwent serious microstrains during the long-term cycling under high-voltage operation, leading to the formation of the micro-cracks and the surface structural

degradation. More importantly, the electrolyte decomposition is significantly increased at such high voltages (≥ 4.5 V), significantly eroding along the surface of these cracks. Therefore, the robustness of the SC-N₈₃ material is greatly boosted by adopting the Zr-doping strategy, which could effectively resist the corrosion of electrolyte and the

considerable volume change at deep charging-discharging process.

4 Conclusion

In summary, we fabricate in situ doping strategy for single-crystal Ni-rich cathode by the combination of co-precipitation and calcination method. The cross-sectional SEM liner scanning and mapping and etch depth XPS reveal that Zr has homogeneous distribution both in surface and bulk of single-crystal $\text{LiNi}_{0.83}\text{Co}_{0.11}\text{Mn}_{0.06}\text{O}_2$. The introduction of trace Zr element could effectively reduce electrochemical polarization. More importantly, the Zr@SC- N_{83} electrode can maintain the structural integrity after long-term cycling even under a high range of 2.75–4.6 V. The in situ doping strategy significantly improves electrochemical performance operating under high-voltage testing condition, which also can provide a guideline for achieving high structural stability of single-crystal Ni-rich cathodes.

Acknowledgements This study was financially supported by the National Natural Science Foundation of China (NSFC, No. 52204328), the Natural Science Foundation of Hunan Province (No. 2022JJ40595), the Scientific Research Fund of Hunan Provincial Education Department (No. 22C0383), China Postdoctoral Science Foundation (No. 2022M713547) and the Science and Technology Innovation Program of Hunan Province (No. 2020SK2007).

Declarations

Conflict of interests The authors declare that they have no conflict of interest.

References

- [1] Goodenough JB, Park KS. The Li-ion rechargeable battery: a perspective. *J Am Chem Soc.* 2013;135(4):1167. <https://doi.org/10.1021/ja3091438>.
- [2] Ji YR, Weng ST, Li XY, Zhang QH, Gu L. Atomic-scale structural evolution of electrode materials in Li-ion batteries: a review. *Rare Met.* 2020;39(03):205. <https://doi.org/10.1007/s12598-020-01369-6>.
- [3] Liu WJ, Sun XZ, Zhang X, Li C, Wang K, Wen W, Ma YW. Structural evolution of mesoporous graphene/ $\text{LiNi}_{1/3}\text{Co}_{1/3}\text{Mn}_{1/3}\text{O}_2$ composite cathode for Li-ion battery. *Rare Met.* 2021;40(3):521. <https://doi.org/10.1007/s12598-020-01406-4>.
- [4] Jung K, Yim T. Calcium-and sulfate-functionalized artificial cathode-electrolyte interphases of Ni-rich cathode materials. *Rare Met.* 2021;40(10):2793. <https://doi.org/10.1007/s12598-021-01710-7>.
- [5] Zhu HK, Yin ZJ, Tang Y, Ren Y, Zhu H, Luo D, Lan S, Yang LG, Liu Q. Modulating precursor nanosheets for stabilized Ni-rich cathode material for Li-ion batteries. *Rare Met.* 2022;41(8):2552. <https://doi.org/10.1007/s12598-022-01983-6>.
- [6] Zeng XL, Li J, Singh N. Recycling of spent lithium-ion battery: a critical review. *Crit Rev Environ Sci Technol.* 2014;44(10):1129. <https://doi.org/10.1080/10643389.2013.763578>.
- [7] Chen M, Zhao E, Chen D, Wu M, Han S, Huang Q, Yang L, Xiao X, Hu ZB. Decreasing Li Ni disorder and improving the electrochemical performances of Ni-rich $\text{LiNi}_{0.8}\text{Co}_{0.1}\text{Mn}_{0.1}\text{O}_2$ by Ca doping. *Inorg Chem.* 2017;56(14):8355. <https://doi.org/10.1021/acs.inorgchem.7b01035>.
- [8] Dahn J. Structure and electrochemistry of $\text{Li}_{1\pm y}\text{NiO}_2$ and a new Li_2NiO_2 phase with the $\text{Ni}(\text{OH})_2$ structure. *Solid State Ionics.* 1990;44:87. [https://doi.org/10.1016/0167-2738\(90\)90049-W](https://doi.org/10.1016/0167-2738(90)90049-W).
- [9] Hayley NY, Li H, Meng YS, Kumar S, Julien B, Clare PG, Yang SH. Changes in the cation ordering of layered $\text{O}_3\text{Li}_x\text{Ni}_{0.5}\text{Mn}_{0.5}\text{O}_2$ during electrochemical cycling to high voltages an electron diffraction study. *Chem Mater.* 2007;19:2551. <https://doi.org/10.1021/cm070139>.
- [10] Jung SK, Gwon H, Hong J, Park KY, Seo DH, Kim H, Hyun J, Yang W, Kang K. Understanding the degradation mechanisms of $\text{LiNi}_{0.5}\text{Co}_{0.2}\text{Mn}_{0.3}\text{O}_2$ cathode material in lithium ion batteries. *Adv Energy Mater.* 2014;4(1):1300787. <https://doi.org/10.1002/aenm.201300787>.
- [11] Xia Y, Zheng J, Wang C, Gu M. Designing principle for Ni-rich cathode materials with high energy density for practical applications. *Nano Energy.* 2018;49:434. <https://doi.org/10.1016/j.nanoen.2018.04.062>.
- [12] Kitchaev DA, Lun Z, Richards WD, Ji H, Clément RJ, Balasubramanian M, Kwon DH, Dai K, Papp JK, Lei T, McCloskey BD, Yang W, Lee J, Ceder G. Design principles for high transition metal capacity in disordered rock salt Li-ion cathodes. *Energy Environ Sci.* 2018;11(8):2159. <https://doi.org/10.1039/C8EE00816G>.
- [13] Lee W, Muhammad S, Kim T, Kim H, Lee E, Jeong M, Son S, Ryou JH, Yoon WS. New insight into Ni-rich layered structure for next-generation Li rechargeable batteries. *Adv Energy Mater.* 2018;8(4):1701788. <https://doi.org/10.1002/aenm.201701788>.
- [14] Aurbach D. The study of electrolyte solutions based on ethylene and diethyl carbonates for rechargeable Li batteries. *J Electrochem Soc.* 1995;142(9):2882. <https://doi.org/10.1149/1.2048659>.
- [15] Chen JG, Vries D, Lewandowski BD, Hall RB. Direct differentiation of surface and bulk compositions of powder catalysts: application of electron-yield and fluorescence-yield NEXAFS to $\text{Li}_x\text{Ni}_{1-x}\text{O}_2$. *Catal Lett.* 1994;23(1–2):25. <https://doi.org/10.1007/BF00812128>.
- [16] Cho DH, Jo CH, Cho W, Kim YJ, Yashiro H, Sun YK, Myung ST. Effect of residual lithium compounds on layer Ni-rich $\text{Li}[\text{Ni}_{0.7}\text{Mn}_{0.3}]\text{O}_2$. *J Electrochem Soc.* 2014;161(6):A920. <https://doi.org/10.1149/2.042406jes>.
- [17] Nohma T, Kurokawa H, Uehara M, Takahashi M, Nishio K, Saito T. Electrochemical characteristics of LiNiO_2 and LiCoO_2 as a positive material for lithium secondary batteries. *J Power Sources.* 1995;54(2):522. [https://doi.org/10.1016/0378-7753\(94\)02140-X](https://doi.org/10.1016/0378-7753(94)02140-X).
- [18] Ohzuku T, Ueda A, Nagayama M, Iwakoshi Y, Komori H. Comparative study of LiCoO_2 , $\text{LiNi}_{12}\text{Co}_{12}\text{O}_2$ and LiNiO_2 for 4 volt secondary lithium cells. *Electrochim Acta.* 1993;38(9):1159. [https://doi.org/10.1016/0013-4686\(93\)80046-3](https://doi.org/10.1016/0013-4686(93)80046-3).
- [19] Kim H, Kim MG, Jeong HY, Nam H, Cho J. A new coating method for alleviating surface degradation of $\text{LiNi}_{0.6}\text{Co}_{0.2}\text{Mn}_{0.2}\text{O}_2$ cathode material: nanoscale surface treatment of primary particles. *Nano Lett.* 2015;15(3):2111. <https://doi.org/10.1021/acs.nanolett.5b00045>.
- [20] Watanabe S, Kinoshita M, Hosokawa T, Morigaki K, Nakura K. Capacity fade of $\text{LiAl}_y\text{Ni}_{1-x-y}\text{Co}_x\text{O}_2$ cathode for lithium-ion batteries during accelerated calendar and cycle life tests (surface analysis of $\text{LiAl}_y\text{Ni}_{1-x-y}\text{Co}_x\text{O}_2$ cathode after cycle tests in restricted depth of discharge ranges). *J Power Sources.* 2014;258:210. <https://doi.org/10.1016/j.jpowsour.2014.02.103>.



- [21] Li YC, Xiang W, Wu ZG, Xu CL, Xu YD, Xiao Y, Yang ZG, Wu CJ, Lv GP, Guo XD. Construction of homogeneously Al³⁺-doped Ni-rich Ni-Co-Mn cathode with high stable cycling performance and storage stability via scalable continuous precipitation. *Electrochim Acta*. 2018;291:84. <https://doi.org/10.1016/j.electacta.2018.08.124>.
- [22] Lim JM, Hwang T, Kim D, Park MS, Cho K, Cho M. Intrinsic origins of crack generation in Ni-rich LiNi_{0.8}Co_{0.1}Mn_{0.1}O₂ layered oxide cathode material. *Sci Rep*. 2017;7:39669. <https://doi.org/10.1038/srep39669>.
- [23] Ryu HH, Park KJ, Yoon CS, Sun YK. Capacity fading of Ni-rich Li[Ni_xCo_yMn_{1-x-y}]O₂ (0.6 ≤ x ≤ 0.95) Cathodes for high-energy-density lithium-ion batteries: bulk or surface degradation? *Chem Mater*. 2018;30(3):1155. <https://doi.org/10.1021/acs.chemmater.7b05269>.
- [24] Wu F, Tian J, Su Y, Wang J, Zhang C, Bao L, He T, Li J, Chen S. Effect of Ni²⁺ content on lithium nickel disorder for Ni-rich cathode materials. *ACS Appl Mater Interfaces*. 2015;7(14):7702. <https://doi.org/10.1021/acsami.5b00645>.
- [25] Fan XM, Ou X, Zhao WG, Liu Y, Zhang B, Zhang JF, Zou LF, Seidl L, Li YZ, Hu GR, Battaglia C, Yang Y. In situ inorganic conductive network formation in high-voltage single-crystal Ni-rich cathodes. *Nat Commun*. 2021;12:5320. <https://doi.org/10.1038/s41467-021-25611-6>.
- [26] Li ZK, Yu XF, Lv YP, Qi L, Yue M, Zhang HZ, Song DW, Shi XX, Zhang LQ. Investigation on the structure and electrochemical performance of LiNi_{0.8}Co_{0.1}Mn_{0.1}O₂ modified with Sn. *Electrochimica Acta*. 2021;400:139468. <https://doi.org/10.1016/j.electacta.2021.139468>.
- [27] Fan XM, Hu GR, Zhang B, Ou X, Zhang JF, Zhao WG, Jia HP, Zou LF, Li P, Yang Y. Crack-free single-crystalline Ni-rich layered NCM cathode enable superior cycling performance of lithium-ion batteries. *Nano Energy*. 2020;70:104450. <https://doi.org/10.1016/j.nanoen.2020.104450>.
- [28] Zhang Z, Bai M, Fan X, Yi M, Zhao YF, Zhang JJ, Hong B, Zhang Z, Hu GR, Lai YQ. A low cost single-crystalline LiNi_{0.60}Co_{0.10}Mn_{0.30}O₂ layered cathode enables remarkable cycling performance of lithium-ion batteries at elevated temperature. *J Power Sources*. 2021;503:230028. <https://doi.org/10.1016/j.jpowsour.2021.230028>.
- [29] Ou X, Liu TC, Zhong WT, Fan XM, Guo XY, Huang XJ, Cao L, Hu JH, Zhang B, Chu YS, Hu GR, Lin Z, Dahbi M, Alami J, Amine K, Yang CH, Lu J. Enabling high energy lithium metal batteries via single-crystal Ni-rich cathode material co-doping strategy. *Nat Commun*. 2022;13:2319. <https://doi.org/10.1038/s41467-022-30020-4>.
- [30] Zhang Z, Hong B, Yi MY, Fan XM, Zhang ZA, Huang XB, Lai YQ. In situ co-doping strategy for achieving long-term cycle stability of single-crystal Ni-rich cathodes at high voltage. *Chem Eng J*. 2022;445:136825. <https://doi.org/10.1016/j.cej.2022.136825>.
- [31] Tian RZ, Wang ZX, Wang XQ, Zhang HZ, Ma Y, Song DW, Shi XX, Zhang LQ. Preparation and electrochemical investigation of single-crystal LiNi_{0.6}Co_{0.2}Mn_{0.2}O₂ for high-performance lithium-ion batteries. *New J Chem*. 2022;46:4877. <https://doi.org/10.1039/D1NJ05359K>.
- [32] Na ZY, Lai C, Zhou J, Zhang HZ, Song DW, Shi XX, Zhang LQ. Enhancing the reversible capacity and cycle stability of lithium-ion batteries with Li-compensation material Li₆CoO₄. *Sci China Mater*. 2022;65(3):620. <https://doi.org/10.1007/S40843-021-1784-0>.
- [33] Yoon CS, Kim UH, Park GT, Kim SJ, Kim KH, Kim J, Sun YK. Self-passivation of a LiNiO₂ Cathode for a lithium-ion battery through Zr doping. *ACS Energy Lett*. 2018;3(7):1634. <https://doi.org/10.1021/acseenergylett.8b00805>.
- [34] Li W, Lee S, Manthiram A. High-nickel NMA: a cobalt-free alternative to NMC and NCA cathodes for lithium-ion batteries. *Adv Mater*. 2020;32(33):2002718. <https://doi.org/10.1002/adma.202002718>.
- [35] Mo W, Wang Z, Wang J, Li X, Guo H, Peng W, Yan G. Tuning the surface of LiNi_{0.8}Co_{0.1}Mn_{0.1}O₂ primary particle with lithium boron oxide toward stable cycling. *Chem Eng J*. 2020;400:125820. <https://doi.org/10.1016/j.cej.2020.125820>.
- [36] Liu FY, Zhang Z, Yu ZY, Fan XM, Yi MY, Bai MH. Bifunctional nitrile-borate based electrolyte additive enables excellent electrochemical stability of lithium metal batteries with single-crystal Ni-rich cathode at 4.7 V. *Chem Eng J*. 2022;434:134745. <https://doi.org/10.1016/j.cej.2022.134745>.
- [37] Aishova A, Park GT, Yoon CS, Sun YK. Cobalt-free high-capacity Ni-rich layered LiNi_{0.9}Mn_{0.1}O₂ cathode. *Adv Energy Mater*. 2020;10:1903179. <https://doi.org/10.1002/aenm.201903179>.
- [38] Yang X, Tang Y, Shang G, Wu J, Lai Y, Li J, Qu Y, Zhang Z. Enhanced cyclability and high-rate capability of LiNi_{0.88}Co_{0.095}Mn_{0.025}O₂ cathodes by homogeneous Al³⁺ doping. *ACS Appl Mater Interfaces*. 2019;11:32015. <https://doi.org/10.1021/acsami.9b10558>.
- [39] Zhang C, Wan J, Li Y, Zheng S, Zhou KE, Wang D, Wang D, Hong C, Gong Z, Yang Y. Restraining the polarization increase of Ni-rich and low-Co cathodes upon cycling by Al-doping. *J Mater Chem A*. 2020;8(14):6893. <https://doi.org/10.1039/D0TA00260G>.
- [40] Dong Z, Wei J, Yue H, Zhang K, Wang L, Li X, Zhang Z, Yang W, Yang S. Multifunctional organosilicon compound contributes to stable operation of high-voltage lithium metal batteries. *J Colloid Interface Sci*. 2021;595:35. <https://doi.org/10.1016/j.jcis.2021.03.058>.
- [41] Mai S, Xu M, Liao X, Hu J, Lin H, Xing L, Liao Y, Li X, Li W. Tris(trimethylsilyl) phosphite as electrolyte additive for high voltage layered lithium nickel cobalt manganese oxide cathode of lithium ion battery. *Electrochim Acta*. 2014;147:565. <https://doi.org/10.1016/j.electacta.2014.09.157>.
- [42] Liu J, Song X, Zhou L, Wang S, Song W, Liu W, Long H, Zhou L, Wu H, Feng C, Guo ZP. Fluorinated phosphazene derivative a promising electrolyte additive for high voltage lithium ion batteries: from electrochemical performance to corrosion mechanism. *Nano Energy*. 2018;46:404. <https://doi.org/10.1016/j.nanoen.2018.02.029>.

Springer Nature or its licensor (e.g. a society or other partner) holds exclusive rights to this article under a publishing agreement with the author(s) or other rightsholder(s); author self-archiving of the accepted manuscript version of this article is solely governed by the terms of such publishing agreement and applicable law.

